This article has been accepted for publication in IEEE Transactions on Power Delivery. This is the author's version which has not been fully edited and content may change prior to final publication. Citation information: DOI 10.1109/TPWRD.2024.3466314

Stability Assessment and Improvement of MTDC System Connected with Offshore Wind Farms

Yin Chen, Lie Xu, *Senior Member, IEEE*, Agustí Egea-Àlvarez, *Member, IEEE*, Eoin Hodge, Shahab Sajedi, Keith McCullough, Paul McKeever, Michael Smailes, *Member, IEEE*

***Abstract*—This paper focuses on the assessment and improvement of the DC network stability of multi-terminal HVDC (MTDC) systems based on Modular Multilevel Converters (MMCs). Therefore, the DC terminal small-signal impedance models for MMCs with different controllers and AC side connections, including onshore AC networks and offshore wind farms (OWFs), are developed in this study. These models are based on the harmonic state space (HSS) method, which accurately captures the internal multi-harmonic couplings of the MMC. Further, by utilizing the impedance models, the paper investigates the effects of different active power controllers and DC cable distances between OWFs, and different DC cable technologies including Cross-linked polyethylene (XLPE) and High-Temperature Superconducting (HTS) cables on the stability of the DC network. To address the negative damping observed in the DC impedance of the MMCs, an improved damping controller implemented with the MMC circulating current controller is proposed to counteract the destabilizing effects and enhance the stability of the DC network. The time-domain simulation results demonstrate the accuracy of the DC impedance models and confirm the effectiveness of the proposed measures for improving system stability.**

Index Terms—MMC, multiterminal HVDC, DC impedance, stability, offshore wind farm, HTS cable.

I. Introduction

Modular multilevel converter (MMC) technology is a competitive solution for integrating large offshore wind farms (OWFs) due to its modularity, low switching loss, and low voltage distortion [1][2]. Over recent years, MMCs have been utilized in many HVDC projects [3][4], and MMC based multi-terminal HVDC (MTDC) systems are already in advanced planning and implementation stages in Europe. However, potential stability issues of future MTDC systems have received increased concerns [5]. MMC-based DC grids are complex systems with multiple ports, and resonances at any AC port can be potentially amplified by the MMC to the DC side, leading to resonance throughout the entire DC grid [6]. Therefore, it is imperative to perform stability analysis to ensure that these oscillations do not compromise the safe operation of the system [7][8].

There are two primary methods for analyzing the small-signal stability of power systems: the state-space method and impedance-based analysis. Compared to the state-space method, impedance-based analysis has the advantage of having "black box" and "plug and play" functions [9], as being widely utilized by both industrial and research communities. In impedance-based analysis, the impedance of the converter is a fundamental and critical requirement. However, developing an accurate impedance model for the MMC has been a significant research challenge due to the steady-state harmonics within the MMC affecting small-signal behavior at both the AC and DC terminals. To address this challenge, the Harmonic State-Space (HSS) method is introduced to develop the MMC AC impedance, which takes into full consideration the influence of harmonics within the MMC on its AC impedance [10]. In MMC, the dynamics of the DC side are intricately linked with those of the AC side due to the interplay of voltage and current interactions, control strategies, energy storage in capacitors. References [11][12] develop the AC impedance model for MMC without considering the impact of the dynamic at the DC terminal. Reference [13] employs the HSS method to construct the DC impedance model for the MMC. Furthermore, in [14], the DC impedance of the MMC connected to OWFs is developed.

Small-signal stability of MTDC systems using two-level VSCs are studied in [15]-[17]. Reference [18] conducts a stability analysis of a three-terminal MMC-HVDC system using the impedance method, whereas in the studied system, two of the MMC's AC terminals are interconnected. Consequently, the study places a specific emphasis on assessing the impact of this AC coupling on the stability. Reference [19] delves into the DC impedance models and characteristics of MMC under various control schemes. The DC impedance models are then used to assess the stability of a four-terminal MTDC system. The study reveals that using a Proportional-Integral (PI) controller for AC power control leads to negative impedance, potentially causing instability issues within the MTDC system. However, the impact of wind farms on system stability is not investigated. References [14][20] take into account the influence of wind farms on the stability at the DC terminal but they primarily focus on point-to-point MTDC configurations. Therefore, previous research has largely concentrated on either point-to-point MMC HVDC or onshore MTDC systems. The stability of MTDC system connected to offshore wind farms, particularly in a meshed structure, has not been thoroughly investigated.

As OWFs grow in scale with long transmission distance, there is an increasing need for them to be connected to onshore

This work was supported by the collaboration project between SuperNode and the Offshore Renewable Energy Catapult (OREC) as part of the research programme of the OREC Electrical Infrastructure Research Hub.

Yin Chen, Lie Xu, and Agustí Egea-Àlvarez are with the Department of Electronic and Electrical Engineering, University of Strathclyde, G1 1XW Glasgow, U.K. (e-mail: yin.chen.101@strath.ac.uk; lie.xu@strath.ac.uk; agusti.egea@strath.ac.uk).

Eoin Hodge, Shahab Sajedi and Keith McCullough are with the SuperNode, Belfield, Dublin 4, Ireland. (e-mail: eoin.hodge@supernode.energy; shahab.sajedi@supernode.energy; keith.mccullough@supernode.energy).

Paul McKeever and Michael Smailes are with the Offshore Renewable Energy Catapult (OREC), NE24 1LZ Blyth, U.K. (e-mail: paul.mckeever@ore.catapult.org.uk; michael.smailes@ore.catapult.org.uk).

This article has been accepted for publication in IEEE Transactions on Power Delivery. This is the author's version which has not been fully edited and content may change prior to final publication. Citation information: DOI 10.1109/TPWRD.2024.3466314

locations via HVDC systems. However, traditional HVDC cables face limitations in current capacity, requiring multiple cables to meet the required transmission capacity. The increased number of cables exacerbates issues related to cost, construction and maintenance difficulty, and environmental impact [21]. An emerging and alternative approach is the use of second-generation high-temperature superconductor (HTS) cables. These HTS cables boast higher current capacity, smaller size, and greater efficiency, and are becoming more practical for industrial use with the availability of commercially viable materials. In recent years, tests and studies have demonstrated the effectiveness of the HTS cables in the power transmission system [22]-[24]. However, compared to XLPE cable, the equivalent resistance of the HTS cable is nearly zero. How this near-zero resistance affects the offshore MTDC system stability has not been studied.

To address these research gaps, this paper investigates the stability challenges of an MMC-based MTDC system connected to OWFs for the first time and develops an enhanced control strategy to improve overall system stability. Firstly, the DC impedances of the MMCs connected to onshore AC grids and OWFs are calculated. Various MMC control strategies, such as grid-forming control for OWF connections, DC and AC voltage regulation, power control, among others, are considered in developing these impedance models. Subsequently, using the impedance model of the MTDC system, the impact of various types of active power control, the location of offshore wind farms, and the application of HTS cables on system stability is thoroughly researched and analyzed. Finally, an MMC active DC damping control method is proposed to enhance overall MTDC system stability. In comparison to previous research, the primary contributions of this paper can be summarized as follows:

1) The impact of different active power controls of the MMC on the DC small-signal behavior and the system stability is investigated. The active power controls include feedforward control, AC power and DC power using PI regulators.

2) The DC side impedance of an MMC connected to an OWF is derived, including the impact of the aggregated OWF, for DC side stability analyses. Based on the DC impedance, the impact of the offshore MMCs on MTDC system stability is studied, which has not been reported before.

3) The impact of HTS cables which has near zero resistance on the MTDC system stability is analyzed.

4) An active damping method based on the circulating current controller of the MMC is adopted to improve MTDC system damping and stability.

The paper is structured in the following manner. Section II describes the four-terminal MTDC system under study, while Section III presents a detailed DC impedance model. Section IV focuses on impedance validation and stability assessments, and Section V investigates the control strategy for improved stability. Finally, Section VI draws the conclusions.

II. MTDC System Configuration

Fig. 1 depicts the schematic diagram of a meshed four-terminal MTDC system, connecting two onshore and two offshore MMCs [25]. The onshore converters, MMC1 and MMC2, are integrated into the AC grids via 352/400 kV transformers. The power generated by each of the two OWFs is transmitted through a 66/200 kV transformer, 200 kV rated AC cables and a 200/352 kV transformer to the offshore MMCs. The meshed 640 kV (±320 kV) DC is formed by the four subsea DC cables, connecting the onshore and offshore stations.

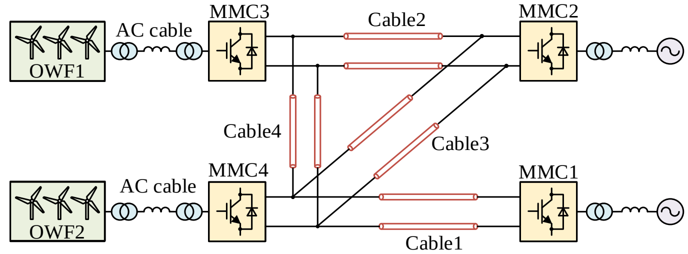

Fig. 1 Meshed four-terminal DC network

A. The configurations of MMC1-4

In the studied system, MMC1-4 have the same structure. The structure and mathematical equations representing the dynamics of the MMCs are detailed in [11] and not repeated here.

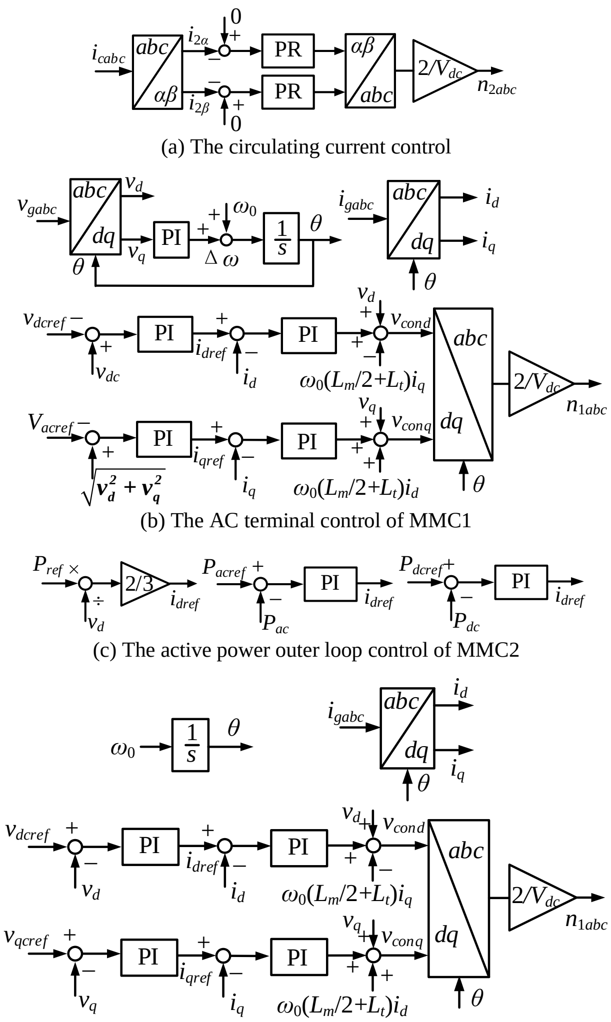

(a) The circulating current control

(b) The AC terminal control of MMC1

(c) The active power outer loop control of MMC2

(d) The AC terminal control of MMC3 and MMC4

Fig. 2 The controllers of MMC1-4

Fig. 2 illustrates the main controllers employed by MMC1-4 in the studied DC network, which are discussed in more details in the following paragraphs. MMC1-4 employ the same circulating current control scheme depicted in Fig. 2(a), which

This article has been accepted for publication in IEEE Transactions on Power Delivery. This is the author's version which has not been fully edited and
content may change prior to final publication. Citation information: DOI 10.1109/TPWRD.2024.3466314

effectively suppresses the circulating current setting the references to 0 and utilizing a Proportional-Resonant (PR) controller tuned at $2\omega_0$ (100 Hz for 50 Hz AC system in this study).

The onshore MMC1 regulates the DC voltage for the MTDC system. Its AC side control is shown in Fig. 2(b), and it is synchronized with the AC grid using a phase-locked loop (PLL). The AC voltages and currents are transformed into a *dq* reference frame based on the phase angle tracked by the PLL. The DC voltage and the magnitude of the three-phase AC voltage are controlled by PI controllers, and the outputs are the *dq* current references (i.e., i_{dref} and i_{qref}) of the inner current loop control.

MMC2 directly controls its active power through the d-axis current, and three different types of active power control are presented in Fig. 2(c). The first type is voltage disturbance feedforward control, where the current setpoint is directly determined by the active power reference and the voltage at the Point of Common Coupling (PCC). This type of control is typically employed to fulfill the operational requirements of the AC grid. The second type is AC active power feedback control using a PI regulator. Unlike feedforward control, it allows for adjustable response speeds of AC active power by tuning the PI parameters [26]. The last type is DC active power feedback control, also utilizing a PI regulator. This type can accurately control the DC power in an MTDC grid [27].

For the offshore MMC3 and MMC4, the controllers are designed to maintain the offshore AC terminal voltage and frequency (e.g., constant V/f control) [14]. As seen, a constant fundamental frequency ω_0 is provided to the controllers in the dq frame. The outer loop control is responsible for regulating v_d and v_q using PI controllers, while the inner current loop regulates the current, as shown in Fig. 2(d).

B. Offshore wind farm

The OWF is represented by an aggregated VSC, and its structure and controller details are depicted in Fig. 3. The components L_f, R_f, and C_f form an RLC filter, which is designed to attenuate the harmonics resulting from PWM switching. Subsequently, the converter is connected to the offshore station through a boost transformer and AC cables. A classic current loop control scheme is adopted, and a PLL is utilized to synchronize the wind farm converter with the offshore AC network.

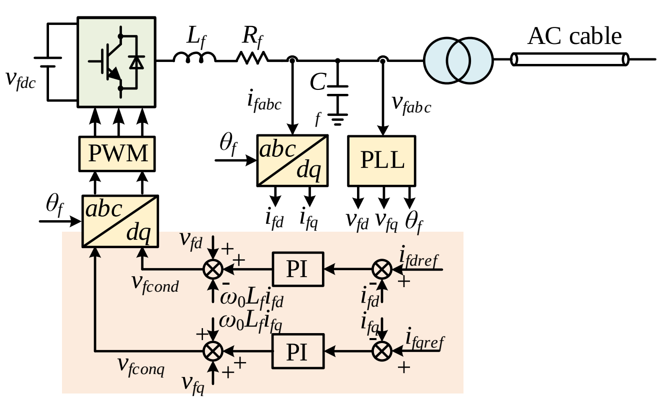

Fig.3 Equivalent converter of the offshore wind farm

III. Small-signal impedance model

A. DC impedance of MMC1

The small-signal model of the MMC in the sequence frame can be expressed as [11]:

$$\begin{cases}\dfrac{d\Delta i_{cpn0}}{dt}=-\dfrac{R_m}{L_m}\Delta i_{cpn0}-\dfrac{N_{upn0}}{2L_m}\Delta v_{cupn0}-\dfrac{N_{lpn0}}{2L_m}\Delta v_{clpn0}-\dfrac{V_{cupn0}}{2L_m}\Delta n_{upn0}\\ \qquad -\dfrac{V_{clpn0}}{2L_m}\Delta n_{lpn0}-\dfrac{1}{2L_m}\Delta v_{dc}\\ \dfrac{d\Delta v_{cupn0}}{dt}=\dfrac{N_{upn0}}{C_m}\Delta i_{cpn0}+\dfrac{N_{upn0}}{2C_m}\Delta i_{gspn0}+\dfrac{I_{cpn0}}{C_m}\Delta n_{upn0}+\dfrac{I_{gspn0}}{2C_m}\Delta n_{upn0}\\ \dfrac{d\Delta v_{clpn0}}{dt}=\dfrac{N_{lpn0}}{C_m}\Delta i_{cpn0}-\dfrac{N_{lpn0}}{2C_m}\Delta i_{gspn0}+\dfrac{I_{cpn0}}{C_m}\Delta n_{lpn0}-\dfrac{I_{gspn0}}{2C_m}\Delta n_{lpn0}\\ \dfrac{d\Delta i_{gspn0}}{dt}=-\dfrac{N_{upn0}}{L_{mac}}\Delta v_{cupn0}+\dfrac{N_{lpn0}}{L_{mac}}\Delta v_{clpn0}-\dfrac{R_m}{L_{mac}}\Delta i_{gspn0}-\dfrac{V_{cupn0}}{L_{mac}}\Delta n_{upn0}\\ \qquad +\dfrac{V_{cupn0}}{L_{mac}}\Delta n_{lpn0}-\dfrac{2}{L_{mac}}\Delta v_{gspn0}\end{cases} \tag{1}$$

where L_m, R_m, and C_m represent the equivalent inductor, resistance, and capacitor on a single arm, respectively. L_t denotes the equivalent inductor of the transformer. The DC voltage is denoted by v_{dc}. In *abc* frame, the three-phase upper and lower arm currents and voltages are represented by i_{uabc}, i_{labc}, v_{uabc}, and v_{labc}, respectively. The modulation ratios for the upper and lower arms are denoted as n_{uabc} and n_{labc}, respectively, which are determined by the controller. v_{cuabc} and v_{clabc} represent the sum of the SM capacitor voltages on the upper and lower arms, respectively. v_{gsabc} represents the AC voltage converted to the converter side of the interface transform, i_{cabc} refers to the three-phase common mode (CM) current circulating internally, while i_{gsabc} represents the differential mode (DM) current flowing into the AC terminal on the converter side of the interface transformer. L_{mac} is the equivalent inductor through which the CM current i_{gsabc} flows, and it is equal to $(0.5L_{arm}+L_t)$. The subscript "*pn*0" represents the positive sequence, negative sequence and zero sequence component in sequence frame. "Δ" denotes small disturbance, and the symbols with the capital letters denote steady-state values.

MMC1 is integrated into the AC grid which is represented by an inductor L_{g1} in series with a resistance R_{g1}. Consequently, the voltage Δv_{gspn0} in (1) can be obtained as:

$$\begin{bmatrix}\Delta v_{gsp}(s)\\ \Delta v_{gsn}(s-2j\omega_0)\end{bmatrix}=\mathbf{Z_{gac}}\begin{bmatrix}\Delta i_{gsp}(s)\\ \Delta i_{gsn}(s-2j\omega_0)\end{bmatrix} \tag{2}$$

$$\mathbf{Z_{gac}}=diag\left[L_{g1}s+R_{g1}\quad L_{g1}(s-2j\omega_0)+R_{g1}\right]/k_t^2$$

where k_t is the voltage ratio of the transformer.

For the PR control in $\alpha\beta$ frame as shown in Fig. 3(a), since the zero-sequence circulating current is not controlled, the transfer function of the circulating current control in sequence frame can be expressed as:

$$\begin{bmatrix}\Delta n_{2p}(s)\\ \Delta n_{2n}(s)\end{bmatrix}=\begin{bmatrix}G_{PR}(s) & 0\\ 0 & G_{PR}(s)\end{bmatrix}\begin{bmatrix}\Delta i_{cp}(s)\\ \Delta i_{cn}(s)\end{bmatrix} \tag{3}$$

$$G_{PR}(s)=K_{rp}+2K_{rr}\zeta\omega_n s/\left(s^2+2\zeta\omega_n s+\omega_n^2\right) \tag{4}$$

The controller of the MMC on the AC terminal in *dq* frame can be derived based on the structure shown in Fig. 3(b) and is generally represented as:

$$\begin{bmatrix}\Delta n_{1d}(s)\\ \Delta n_{1q}(s)\end{bmatrix}=\mathbf{G_{idq}}\begin{bmatrix}\Delta i_{gd}(s)\\ \Delta i_{gq}(s)\end{bmatrix}+\mathbf{G_{vdq}}\begin{bmatrix}\Delta v_{gd}(s)\\ \Delta v_{gq}(s)\end{bmatrix}+\begin{bmatrix}G_{vdc}(s)\\ 0\end{bmatrix}\Delta v_{dc}(s) \tag{5}$$

This article has been accepted for publication in IEEE Transactions on Power Delivery. This is the author's version which has not been fully edited and content may change prior to final publication. Citation information: DOI 10.1109/TPWRD.2024.3466314

where the controller of MMC1 on the AC terminal in the *dq* frame is characterized by the transfer functions $\mathbf{G_{idq}}$ and $\mathbf{G_{vdq}}$, which describe the relationship between the AC current Δi_g, AC voltage Δv_g, and the DM components of the modulation ratio Δn_1. Additionally, there is a transfer function G_{vdc} associated with the DC voltage controller. These transfer functions are typically derived and represented in the *dq* frame.

To incorporate the controllers into the MMC model, it is necessary to transform the transfer functions from the dq frame to the sequence frame. The relationship between the components in the *dq* frame and the components in the sequence frame is established through appropriate mathematical transformations given as [28]:

$$\begin{bmatrix} x_d(t) \\ x_q(t) \end{bmatrix} = \begin{bmatrix} 1 & 1 \\ -j & j \end{bmatrix} \begin{bmatrix} e^{-j\omega_0 t} & 0 \\ 0 & e^{j\omega_0 t} \end{bmatrix} \begin{bmatrix} x_p(t) \\ x_n(t) \end{bmatrix} \tag{6}$$

Transforming (5) into sequence frame based on (6) and combining (2) yields:

$$\begin{bmatrix} \Delta n_{1p}(s) \\ \Delta n_{1n}(s-2j\omega_0) \end{bmatrix} = (\mathbf{G_{ipn}} + \mathbf{G_{vpn}}\mathbf{Z_{gac}}) \begin{bmatrix} \Delta i_{gp}(s) \\ \Delta i_{gn}(s-2j\omega_0) \end{bmatrix} + \mathbf{G_{vdc}} \Delta v_{dc}(s-j\omega_0) \tag{7}$$

where the matrices $\mathbf{G_{ipn}}$, $\mathbf{G_{vpn}}$ and $\mathbf{G_{vdc}}$ are the transfer functions of the controller in sequence frame. It is found that the positive-sequence current Δi_{gp} with frequency ω_p, the negative-sequence current Δi_{gn} with frequency (ω_p-2ω_0) and the DC voltage Δv_{dc} with frequency (ω_p-ω_0) are coupled together through the DC voltage control implemented on the MMC AC terminal.

The relationship between the MMC DC current Δi_{dc} and the circulating current Δi_c can be depicted as [20]:

$$\Delta i_{dc}(s) = 3\Delta i_{c0}(s) \tag{8}$$

where Δi_{c0} is the zero-sequence component of the circulating current.

By substituting (2) and (7) into (1) and then expanding it, the HSS model of the MMC can be obtained. The process of establishing the HSS model has been extensively discussed in [10] and [11], and is not reiterated here.

By solving the HSS model and combining (8), the MMC DC small-signal impedance can be derived as:

$$Z_{MMC1}(s-j\omega_0) = \Delta v_{dc}(s-j\omega_0) / \left[3\Delta i_{c0}(s-j\omega_0)\right] \tag{9}$$

This impedance characterizes the small-signal behavior of the MMC system on the DC terminal with considering the AC circuit connected with the MMC.

B. DC impedance of the onshore MMC2

In MMC2, active power control is implemented on the d-axis in the dq frame. Three different active power control strategies depicted in Fig. 2(c) are investigated. Among these strategies, feedforward control and P_{ac} with PI controller have similar transfer function structures, with inputs including Δi_{gd}, Δi_{gq}, Δv_{gd}, and Δv_{gd}. The transfer functions for these two controllers follow the general expression shown in (5). Therefore, similar procedures can be applied to derive the small-signal impedance at the DC terminal.

The small-signal expression of DC power is expressed as:

$$\Delta P_{dc} = V_{dc}\Delta i_{dc} + I_{dc}\Delta v_{dc} \tag{10}$$

where V_{dc} and I_{dc} are the steady-state value of the DC voltage and current, respectively.

By combining (2), (6), (8) and (10), the transfer function of the AC terminal control including the P_{dc} control loop can be expressed as:

$$\begin{bmatrix} \Delta n_{1p}(s) \\ \Delta n_{1n}(s-2j\omega_0) \end{bmatrix} = (\mathbf{G_{ipn}} + \mathbf{G_{vpn}}\mathbf{Z_{gac}}) \begin{bmatrix} \Delta i_{gp}(s) \\ \Delta i_{gn}(s-2j\omega_0) \end{bmatrix} + \mathbf{G_{Pdcv}} \Delta v_{dc}(s-j\omega_0) + \mathbf{G_{Pdci}} \Delta i_{c0}(s-j\omega_0) \tag{11}$$

where

$$\mathbf{G_{Pdcv}} = \left[I_{dc}G_{Pdc}(s-j\omega_0)/2,\ I_{dc}G_{Pdc}(s-j\omega_0)/2\right]^T \tag{12}$$

$$\mathbf{G_{Pdci}} = \left[3V_{dc}G_{Pdc}(s-j\omega_0)/2,\ 3V_{dc}G_{Pdc}(s-j\omega_0)/2\right]^T \tag{13}$$

Comparing to the DC voltage control described in (7), the transfer function of P_{dc} control incorporates not only Δi_{gpn}, Δv_{gpn}, and Δv_{dc} but also the zero-sequence component of the circulating current Δi_{c0}. By substituting the submatrices of the transfer functions $\mathbf{G_{ipn}}$+$\mathbf{G_{vpn}Z_{gac}}$, $\mathbf{G_{pdcv}}$, and $\mathbf{G_{pdci}}$, as specified in (11), into (1), the MMC HSS model can be derived. Using the HSS model, the DC impedance of MMC2 with P_{dc} control can then be calculated.

C. DC impedance of the offshore MMC3 and MMC4.

In order to accurately characterize the DC behavior of MMC3 and MMC4, it is necessary to take into account the influence of the OWFs on their AC sides by considering the equivalent AC impedance of the OWFs. Based on [10] and [14], the impedance matrix Z_{OWFpn} of the OWF can be obtained. This matrix is a 2 by 2 off-diagonal matrix in sequence frame that describes the interdependence between small-signal positive-sequence and negative-sequence currents and voltages at different frequencies.

When OWFs are interconnected with MMC3 and MMC4, the AC impedance connected with the MMC are expressed as:

$$Z_{opn} = Z_{OWFpn} / k_{ot}^2 + Z_{otpn} + Z_{ACcabpn} \tag{14}$$

where Z_{otpn} represents the impedance of the boosting transformer connected with the OWF, and $Z_{ACcabpn}$ is the impedance of the AC cables shown in Fig. 3. Noted that (14) is a simplified representation, while the shunt capacitors of AC cables are considered when calculating the overall impedance Z_{opn}, which is an off-diagonal matrix and differs from the diagonal matrix Z_{gac} of the AC grid impedance in (2). To account for the frequency coupling of Z_{OWFpn}, each element of Z_{opn} is rearranged in the MMC HSS model. This rearrangement ensures that the small-signal behavior of the offshore MMCs at the DC terminal accurately captures the influence of the frequency coupling characteristics of the OWFs.

By following the similar procedures in Section III A, the transfer functions of the AC terminal controllers for MMC3 and MMC4 can be derived. Subsequently, the DC impedances Z_{MMC3} and Z_{MMC4} can be obtained.

D. Impedance of AC and DC cable

For the traditional DC cables, it is recommended to use a parallel branch section rather than π-section for improving the accuracy of replicating universal line model (ULM) behavior [29]. One section is shown in Fig. 4.

This article has been accepted for publication in IEEE Transactions on Power Delivery. This is the author's version which has not been fully edited and content may change prior to final publication. Citation information: DOI 10.1109/TPWRD.2024.3466314

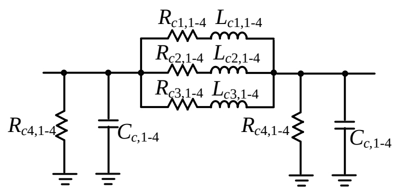

Fig.4 one single parallel branch section

Reference [29] demonstrates that five π-sections are sufficient to capture the dynamic characteristics of a long DC cable. To ensure the model's accuracy, the use of five sections has been implemented in this work. As the cables have different lengths, the parameters of one section for the DC Cable 1-4 are different and represented as $R_{c1,1\text{-}4}$, $R_{c2,1\text{-}4}$, $R_{c3,1\text{-}4}$, $R_{c4,1\text{-}4}$, $L_{c1,1\text{-}4}$, $L_{c2,1\text{-}4}$ and $C_{c,1\text{-}4}$. On the other hand, the offshore AC cable, which is significantly shorter in length compared to the DC cable in the HVDC transmission system and have a minor impact on the stability of the DC network, is represented using two π-sections.

E. DC network impedance model for stability assessment

For the MTDC system shown in Fig. 1, stability analysis can be conducted at each DC terminal of the MMCs using impedance-based method. Taking MMC3 as an example, when considering the DC terminal, the DC impedance Z_{MMC3} of MMC3 is derived in Section III C. The rest of the overall network of the DC system can then be represented by the equivalent impedance Z_{net3} as illustrated in Fig. 5. Each DC cable is represented by five parallel branch sections connected in series. The values of $Z_{c1\text{-}4}$ and $Y_{c1\text{-}4}$ for the four DC cables can be calculated based on a single parallel section depicted in Fig. 4. Then, Z_{net3} can be obtained by the node voltage equations.

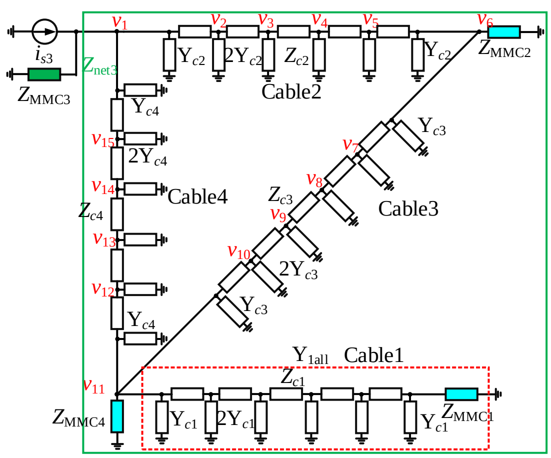

Fig. 5 The impedance model of the MTDC system

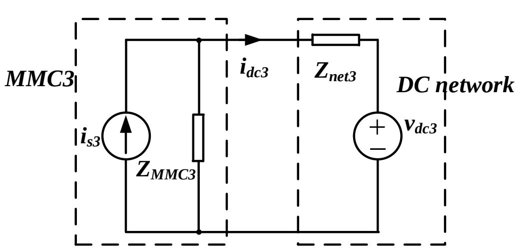

Fig. 6 Small-signal equivalent circuit of MTDC system at MMC3.

Since MMC3 operates as a rectifier with DC current flowing into the DC network and the DC voltage maintained by the other converters in the MTDC system, MMC3 can be modeled as a current source in parallel with Z_{MMC3}. The rest of the overall network of the DC system can then be represented by the equivalent impedance Z_{net3} in series with a voltage source, as illustrated in Fig. 6. The DC current i_{dc3} flowing from MMC3 to the DC network is given by:

$$i_{dc3}(s)=\left[i_{s3}(s)-v_{dc3}(s)/Z_{MMC3}(s)\right]/\left[1+Z_{net3}(s)/Z_{MMC3}(s)\right] \quad (15)$$

where $i_{s3}(s)$ and $v_{dc3}(s)$ are the equivalent sources of MMC3 and DC network, respectively. The stability analysis of the MTDC system at the MMC3 terminal can then be conducted by evaluating the Nyquist curve of $Z_{net3}(s)/Z_{MMC3}(s)$, taking into account the right-half-plane (RHP) poles of $Z_{net3}(s)$ and the zeros of $Z_{MMC3}(s)$ [30]. It is important to note that for the MTDC system, the stability at each converter connection point must be examined.

IV. Impedance Validation and Case Study

The system parameters are listed in Tables I-III.

TABLE I
ELECTRICAL PARAMETERS OF MMCS AND OWFS

MMC1-4		OWF1,2	
Rated Active Power	1000 MW	Rated Active Power	1000 MW
Rated AC Voltage	360 kV	Rated AC Voltage	69 kV
Arm Inductance (L_m)	83.5 mH	Filter Inductance (L_f)	2.3 mH
Arm Resistance (R_m)	0.07 Ω	Filter Resistance (R_f)	0.024 Ω
Arm Capacitance (C_m)	32.34 μF	Filter Capacitance (C_f)	100.3μF
Connected Transformers			
Rated Power	1270 MVA	Rated Power	1270 MVA
Voltage Ratio onshore (k_t)	400/352	Voltage Ratio (k_{ot})	200/69
Voltage Ratio offshore (k_t)	200/352		
Leakage Inductance (L_t)	0.12 pu	Leakage Inductance (L_{ot})	0.12 pu
AC grid SCR	5	AC grid X/R	10

TABLE II
DC AND AC CABLE PARAMETERS

XLPE DC cable			
R_{c1}	0.0633 Ω/km	L_{c1}	0.2522 mH/km
R_{c2}	0.0752 Ω/km	L_{c2}	7.7346 mH/km
R_{c3}	0.0089 Ω/km	L_{c3}	3.7956 mH/km
$1/R_{c4}$	0.2334 μS/km	C_c	0.3564 μF/km
HTS DC cable			
L_{HTS}	0.268 mH/km	C_{HTS}	0.219 μF/km
Lengths of DC cables			
Cable 1	160 km	Cable 3	175 km
Cable 2	150 km	Cable 4	65 km
Offshore AC cable			
R_{ac}	0.0109 Ω/km	L_{ac}	0.41 mH/km
C_{ac}	0.173 μF/km	Length	6 km

TABLE III
CONTROLLER PARAMETERS OF MMC1-4

<table>
<tr><th></th><th>MMC1</th><th>MMC2</th><th>MMC3</th><th>MMC4</th></tr>
<tr><td>Current loop K_{ip}/K_{ii}</td><td colspan="4">0.65 / 100 (pu)</td></tr>
<tr><td>CCC $K_{rp}/K_{rr}/\zeta$</td><td colspan="4">0.8 / 100 / 0.01 (pu) [32]</td></tr>
<tr><td>PLL K_{pllp}/K_{plli}</td><td colspan="2">250 / 5000 (pu)</td><td colspan="2" rowspan="3">N/A</td></tr>
<tr><td>AC voltage control K_{up}/K_{ui}</td><td colspan="2">1 / 10 (pu)</td></tr>
<tr><td>DC voltage control K_{dcp}/K_{dci}</td><td>4 / 50 (pu)</td><td>N/A</td></tr>
<tr><td>d- and q-axis voltage control K_{vp}/K_{vi}</td><td colspan="2">N/A</td><td colspan="2">5 / 100 (pu)</td></tr>
</table>

In this study, AC cables have been minimized since its impact on the DC side stability is minimal. The parameters of the DC cables are obtained from experimental measures, and the parameters of the equivalent ULM are derived according to [31].

In Figs. 7 and 8, the solid lines represent the DC impedances of the MMCs with different controllers, calculated using the analytical models developed in Section III, while the dots represent the measured impedances obtained from time-domain simulations using frequency scanning. As shown, the dots overlap with the lines, validating the accuracy of the developed MMC DC impedance models.

A. Different active power controllers for MMC2

In the case of low wind condition and MMC2 operating as a rectifier (feeding power to MMC1), OWF1 and OWF2 generate 0.2 GW and 0.15 GW of active power, respectively, which are transmitted through offshore MMC3 and MMC4 converters into the DC network. The onshore MMC2 injects 0.65 GW of active power into the DC network, while MMC1 with DC voltage control absorbs almost 1 GW of active power from the DC network to its AC side. The XLPE cables are used in this case.

The DC impedances of MMC1- MMC4 are illustrated in Fig. 7, with MMC2 using active power feedforward control, i.e., ($2P_{ref}/3v_d$). For MMC1, which adopts DC voltage control, the black line in Fig. 7 exhibits lowest magnitudes at low frequencies when compared to MMC2, MMC3 and MMC4. At frequencies above 200 Hz, Z_{MMC1}, Z_{MMC2}, Z_{MMC3}, and Z_{MMC4} have similar magnitude and phase. This is because the controller of the MMC has a negligible effect on the small-signal behavior of the DC current and voltage. As a result, the DC impedance at high frequency is equal to the total impedance of the upper and lower three-phase bridge arms, i.e., $2(L_m+R_m)/3$.

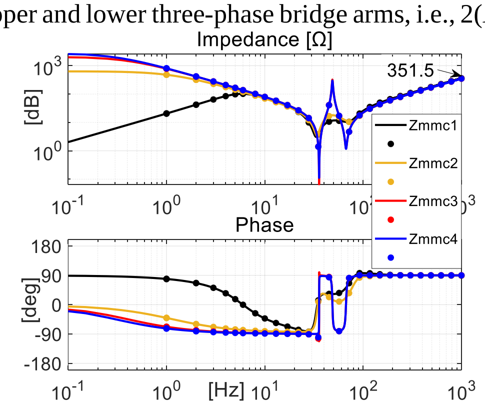

Fig. 7 DC impedances of MMC1-4.

Fig. 8 illustrates the DC impedances of MMC2 under different active power control schemes shown in Fig. 3(c) and different parameter settings. The integral gains, K_{iac} and K_{idc}, are set to 40 times the proportional gains, K_{pac} and K_{pdc}, respectively. When K_{pac} and K_{pdc} are altered, K_{iac} and K_{idc} are adjusted accordingly. It is noteworthy that regardless of the active power control type, all impedances exhibit identical magnitudes at very low frequencies, approximately 633 Ω, which is approximately equal to the DC impedance under steady-state conditions, i.e., (640 kV)^2/(0.65 GW). Moreover, the phase angle is almost 0°, indicating a resistive impedance. At higher frequencies (above 200 Hz), all impedances become inductive and are equal to $2(L_m+R_m)/3$, consistent with Z_{MMC1}, Z_{MMC3}, and Z_{MMC4} depicted in Fig. 7.

In Fig. 8(a), varying the gains of the P_{ac} controller results in impedances that are identical at most frequencies, apart from frequencies around 35-90 Hz, suggesting that the system response remains almost the same across these ranges. Some impedance differences are observed between 35-90 Hz. As the control gain increases, the impedance magnitude and phase exhibit minor difference, i.e., higher peaks and lower valleys. However, the phase angles of the impedances still range between ±90°, indicating positive damping and beneficial characteristics for system stability.

As shown in Fig. 8(b), despite the P_{dc} controller having a much smaller control parameter value, it exhibits larger impedance magnitude values compared to the impedance with feedforward control below 30 Hz. Moreover, in this frequency range, the frequency responses of Z_{MMC2} exhibit characteristics similar to that of a low pass filter. With increased P_{dc} control parameters, the "cutoff frequency" of Z_{MMC2} also increases, resulting in a faster response during dynamic events. However, the phase angle becomes lower than -90°, indicating negative damping and reduced stability. Notably, when K_{pdc} is set to 1 pu, the phase angle of the impedance in the frequency range of 5-30 Hz and 50-100 Hz falls to the range of 90°-270°, which further signifies negative damping and potential stability concerns.

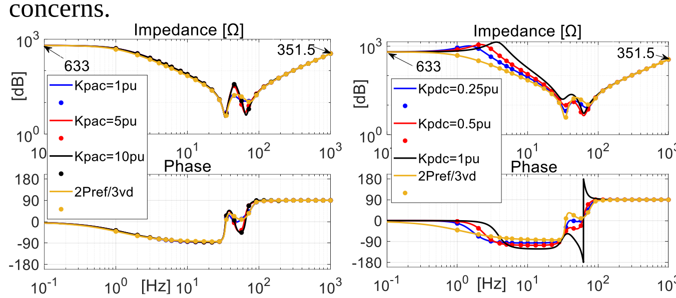

(a) Feedforward and P_{ac} control (b) Feedforward and P_{dc} control

Fig. 8 MMC2 DC impedances with different control and parameters

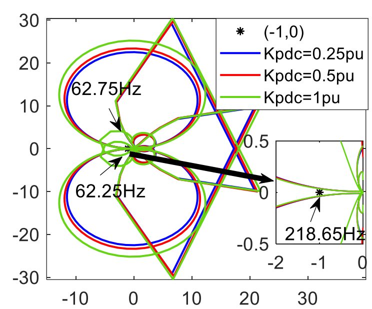

Fig. 9 The Nyquist curves of $Z_{net3}(s)/Z_{MMC3}(s)$ with different K_{pdc}

The stability assessment with MMC2 under P_{dc} control is conducted, and the Nyquist curves are depicted in Fig. 9. As seen, when K_{pdc} is set to 0.25 pu and 0.5 pu, the blue and red curves do not encircle the point (-1, 0), indicating stable system. However, both curves come very close to the (-1, 0) point at a frequency of 218.65 Hz, suggesting weak damping around 218 Hz. In contrast, when K_{pdc} is increased to 1 pu, the green curve encircles the point (-1, 0) with corresponding frequencies ranging from 62.25-62.75 Hz. This indicates system instability, and the resonant frequency is estimated to be around 63 Hz.

To validate the analysis results obtained from the impedance model, EMT simulations in the time domain are conducted in Matlab/Simulink. The system settings remain consistent with

This article has been accepted for publication in IEEE Transactions on Power Delivery. This is the author's version which has not been fully edited and content may change prior to final publication. Citation information: DOI 10.1109/TPWRD.2024.3466314

the description provided at the beginning of this section. Average MMC models are used, and the DC cable is modeled using the ULM.

Fig. 10 depicts the DC active power responses when a small DC current perturbation is introduced through an additional parallel current source on MMC2 DC terminal at 9 s. The responses with different P_{ac} control parameters exhibit nearly identical behavior to the active power feedforward control. Specifically, the active power undergoes low-frequency oscillations (approximately 2.5 Hz) before reaching its final steady state. This observation is consistent with the impedance analysis in Fig. 8(a), which demonstrates that variations in P_{ac} control do not affect the small-signal behavior of the DC active power.

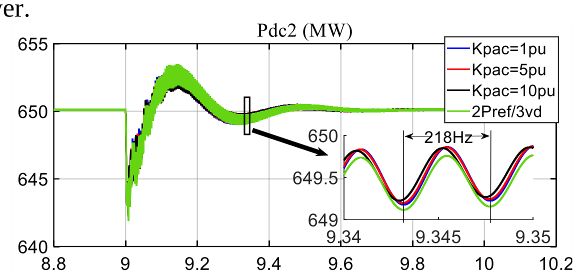

Fig.10 MMC2 active power response with P_{ac} control and feedforward control.

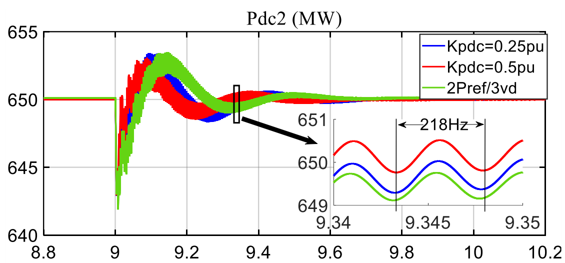

(a) Stable with K_{pdc}=0.25 pu and K_{pdc}=0.5 pu

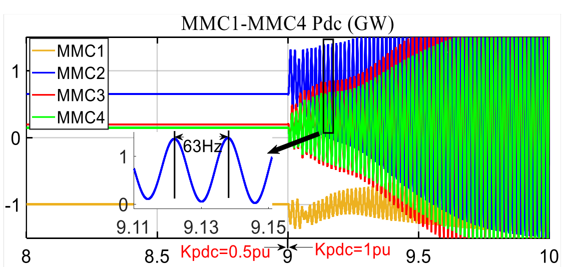

(b) Stable with K_{pdc}=0.5 pu and unstable with K_{pdc}=1 pu

Fig.11 MMC2 active power response with P_{dc} control and feedforward control.

Fig. 11 illustrates the DC active power responses under P_{dc} control. As depicted in Fig. 11(a), the responses under P_{dc} control exhibit faster dynamics compared to those under active power feedforward control. Moreover, with higher P_{dc} control parameters, the response becomes quicker. However, when K_{pdc} increases to 1 pu, the system becomes unstable with a resonant frequency of 63 Hz, as shown in Fig. 11(b). These simulation results are consistent with the analysis findings from impedances in Figs. 8(b) and 9, indicating that higher P_{dc} control parameters result in faster responses of the DC active power but may introduce stability issues at the DC terminal.

Moreover, all the responses in Figs. 10 and 11(a) display 218 Hz ripples and exhibit slow damping. This observation again aligns with the impedance analysis in Fig. 8, where the MMC DC impedance at 218 Hz is equivalent to $2(L_m+R_m)/3$ and resonates with the DC cable due to the limited damping at 218 Hz. This resonance phenomenon is also evident in the Nyquist curves presented in Fig. 9, where all Nyquist curves at 218.65 Hz closely approach the critical point (-1, 0).

Similar findings are obtained when MMC2 operates in the inverter mode with various active power levels, but these results are not reiterated here.

B. Different distances between the offshore stations

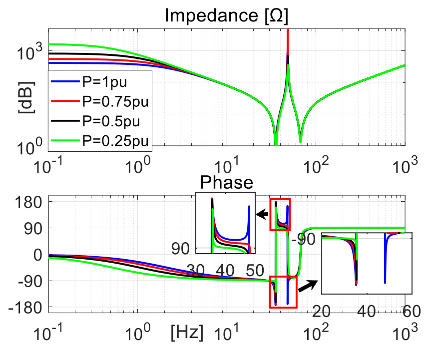

Fig.12 MMC3 DC impedances with different power flows.

The DC impedances of the offshore converter, specifically MMC3 and MMC4, with different transmitted active powers from the OWFs into the DC network are depicted in Fig. 12. It can be observed that due to the variation in transmitted active power, the impedances at low frequencies differ. Additionally, at higher active power levels, more parts of the phase fall outside the range of -90° to 90° between 20-60 Hz, meaning higher negative resistance, which poses a potential risk to system stability [33]. Since both OWFs have a similar structure, the impedance Z_{MMC4} is approximately equal to Z_{MMC3} and is not presented again.

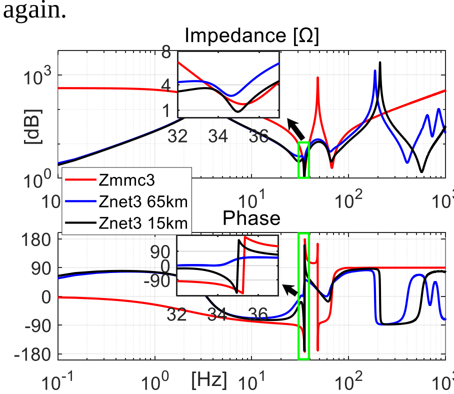

(a) System DC impedances

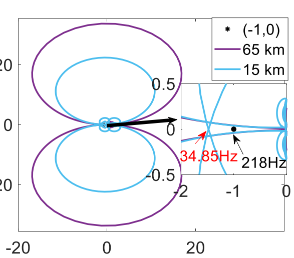

(b) Nyquist curves

Fig.13 Analysis with different lengths of Cable 4.

When the active power is 1 GW and the DC cable length between MMC3 and MMC4 is 15 km and 65 km respectively, the impedance of MMC3 Z_{MMC3} and the network equivalent

This article has been accepted for publication in IEEE Transactions on Power Delivery. This is the author's version which has not been fully edited and content may change prior to final publication. Citation information: DOI 10.1109/TPWRD.2024.3466314

impedance seen from the MMC3 terminal Z_{net3} are shown in Fig. 13(a). For the 15 km cable length, Z_{MMC3} intersects with Z_{net3} around 35 Hz, and Z_{net3} exhibits negative resistance. Inversely, for the 65 km cable length, Z_{net3} has positive resistance, contributing to system stability.

The corresponding Nyquist curves are presented in Fig. 13(b). It is clearly evident that the system remains stable when the cable length is 65 km. However, when the cable length is reduced to 15 km, the system becomes unstable, with a resonant frequency of approximately 34.85 Hz. Furthermore, weak damping is also observed at around 218 Hz caused by the resonance between the MMCs' arm impedances and DC cables, which was also observed in Fig. 9.

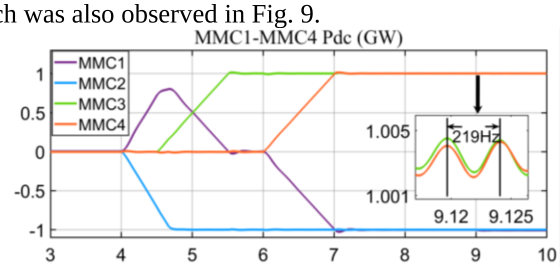

Fig. 14 The active power of MMC1-4 with 65 km Cable 4

Fig. 14 depicts the time-domain simulation for the scenario where Cable 4 has a length of 65 km. The stability of the system in simulation supports the validity of the impedance model analysis. However, the unstable simulation result associated with a 15 km cable length will be presented in Section V.

C. DC network with HTS cable at rated power

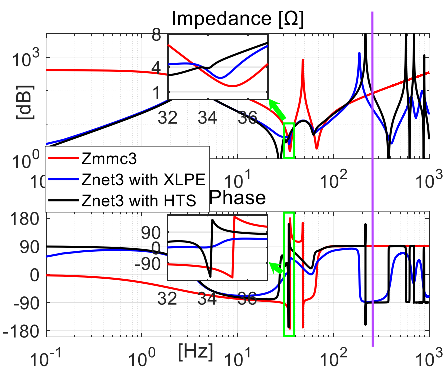

Fig. 15 The DC impedances with XLPE cables and HTS cables.

In Section IV B, it concludes that the DC network remains stable with the XLPE cables connection when MMC3 is positioned far away from MMC4. The same condition is maintained, but the normal DC cables are replaced with the HTS cables which have ignorable resistances [34]. Fig. 15 compares the impedance Z_{MMC3} and the network impedance Z_{net3} with XLPE cables and HTS cables. It can be observed that Z_{MMC3} intersects with Z_{net3} (with HTS cable) at around 34 Hz, while both impedances exhibit negative resistance in this frequency range. The negative resistances potentially lead to stability issues in the system. Additionally, there is another intersection at 256 Hz (purple line in Fig. 15). At this frequency, Z_{MMC3} is predominantly inductive, approximately equal to $2(L_m+R_m)/3$ at high frequencies, while Z_{net3} with HTS cable is mostly capacitive since the damping in Z_{net3} is only provided by the arm resistances of MMC1, MMC2, and MMC4, which are very small. Consequently, the DC network exhibits extremely weak damping at 256 Hz, and the damping is lower than that at 218 Hz with XLPE cables because the resistances of the XLPE cables provide positive damping effect.

Fig. 16 depicts the Nyquist curve when the HTS cables are implemented. Due to the near-zero resistance of the HTS cable, Z_{net3} has sharp resonance points above 100 Hz, characterized by high magnitude and extremely sharp phase changes. This results in the spikes in the Nyquist curve shown in Fig. 16. Moreover, the curve encircles the point (-1, 0), indicating that the system is unstable. To validate these findings, time-domain simulations are presented in the next section.

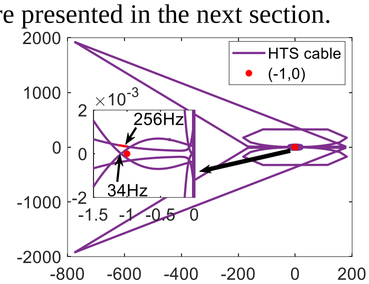

Fig. 16 The Nyquist curve with HTS cables.

D. DC network with HTS cable at low transmitted power

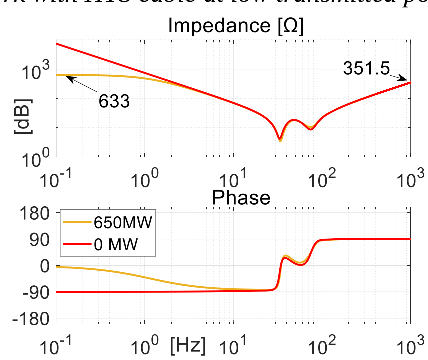

Fig. 17 MMC2 DC impedances with different transmitted power.

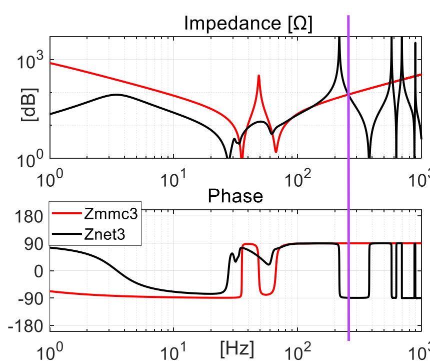

Fig. 18 The DC impedances with HTS cables at low transmitted power.

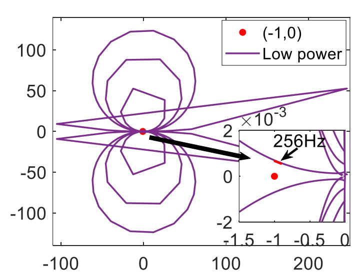

Fig. 19 The Nyquist curve with HTS cables at low transmitted power.

In this scenario, each OWF generates 200 MW (0.2 pu) of active power, which is transmitted through the DC network using HTS cables. MMC2 employs feedforward control and absorbs 0 MW from the DC network. Thus, MMC1, which is

This article has been accepted for publication in IEEE Transactions on Power Delivery. This is the author's version which has not been fully edited and content may change prior to final publication. Citation information: DOI 10.1109/TPWRD.2024.3466314

under DC voltage control, absorbs 400 MW (0.4 pu) from the DC network. The DC impedance of MMC2 with feedforward control in this scenario is compared to that in Fig. 8 and is shown in Fig. 17. The main differences of the impedance occur in the low frequency range. With 650 MW, the magnitude of MMC2 impedance at low frequency, represented by the yellow line in Fig. 17, is approximately (640 kV) ^2/ (0.65 GW) = 630 Ω. In contrast, with 0 MW, the magnitude of MMC2 impedance at low frequency, shown by the red line in Fig. 17, is extremely high. This near-infinite impedance at DC causes the power flowing through MMC2 to be zero.

The DC impedance of MMC3 and the network impedance Z_{net3} are shown in Fig. 18. Compared with the impedances in Fig. 15, it can be observed that when the active power of the OWF is reduced, the negative resistance of Z_{MMC3} at around 30 Hz disappears, which prevents the stability issue in this frequency range. However, at around 250Hz, there is still an intersection of the magnitudes of Z_{MMC3} and Z_{net3}. Moreover, at this frequency, Z_{MMC3} is purely inductive and Z_{net3} is purely capacitive. These characteristics result in a resonant system. The Nyquist curve presented in Fig. 19 confirms the analysis based on impedances. At around 256 Hz, the Nyquist curves are extremely close to (-1,0), indicating critical stability at 256 Hz.

V. Improve System Stability

The negative resistance effect of the MMC DC impedance can cause instability in the DC network. This challenge can become more pronounced when using HTS cables with negligible DC resistance. To improve system stability, it is necessary to introduce positive resistance at concerned frequencies. As the DC current is linked to the zero-sequence component of the MMC circulating current, as indicated in (8), the zero-axis control of circulating current in αβ0 frame or dq0 frame can significantly affect the DC impedance of MMC. Fig. 20 illustrates the proposed circulating current control, which aims to improve the system stability.

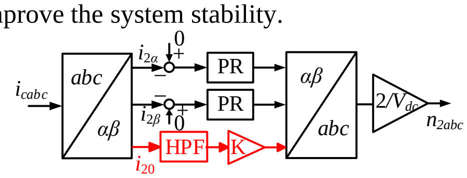

Fig. 20 Proposed zero-sequence controller of the circulating current.

As seen, the zero-sequence controller of the circulating current consists of a high pass filter (HPF) and a gain. The HPF ensures that the controller has limited impact on the DC (low frequency) components of the circulating current, allowing adequate DC response. The gain, represented by the symbol K, is used to introduce a virtual resistance at specified frequencies, which is added to the system in order to counteract the negative resistance to improve the stability of the DC network. For the HPF, the gain at high frequencies is equal to K, which means a virtual resistance of K Ω is added to each arm of the MMC. Consequently, for the DC terminal of the MMC, the additional virtual resistance is 2K/3 Ω. It is noted that in [12] the similar controller is investigated to improve the AC impedance through the harmonic coupling within the MMC. However, the zero-sequence component of the MMC circulating current directly affects the DC current. Therefore, using this controller to reshape DC impedance is a more straightforward and effective approach.

A. Improving system stability with P_{dc} Control

In Fig. 8(b), it is observed that when the proportional gain K_{pdc} of MMC2 is set to 1 pu, the DC impedance of MMC2 exhibits negative resistance in the frequency range of 5-100 Hz. This negative resistance causes instability in the DC system, particularly at 63 Hz. To address this instability and improve system stability, the proposed control strategy is implemented in MMC2. The proposed control strategy utilizes a second order HPF with a cutoff frequency of 20 Hz and a damping ratio ζ of 0.707. The gain factor K is set to 15.

Fig. 21 illustrates the impedance characteristics with and without the proposed controller. As seen, when the proposed controller is applied, the negative resistance effect is eliminated in the frequency range of 30-100 Hz. Moreover, the impedance phase is reduced in the frequency range of 200-250 Hz. This reduction indicates that the weak damping at 218 Hz shall also be improved with the proposed controller.

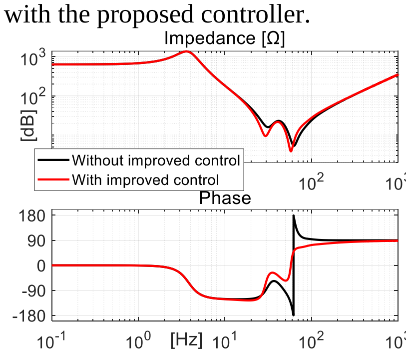

Fig. 21 Z_{MMC2} with and without proposed control.

The time-domain simulation result is presented in Fig. 22. Prior to 9.5 s, the proposed controller is applied with a K_{pdc} value of 1 pu, and the system remains stable. At 9 s, a disturbance is introduced at the DC terminal of MMC2 to assess the weak damping frequency. In comparison to the results shown in Figs. 10 and 11(a), the presence of the proposed controller in Fig. 22 eliminates the high-frequency ripple at 218 Hz. This is due to the additional positive damping provided by the proposed control strategy. However, at 9.5 s, MMC2 reverts to its original circulating current controller, and as a result, the stability of the system deteriorates.

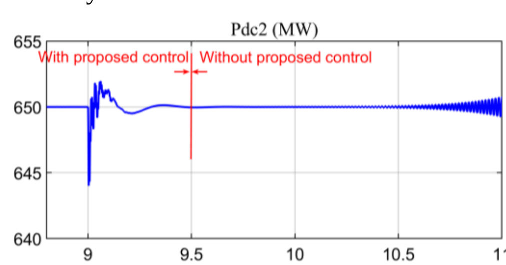

Fig. 22 With and without proposed control when K_{pdc}=1.

B. Improving system stability with OWFs in close proximity

In Section IV B, the analysis revealed that the DC network would become unstable when the two offshore stations are located closely, e.g., at 15 km. To address this instability, the proposed controller is implemented for MMC3, and Fig. 23 illustrates the impedance Z_{MMC3}, clearly demonstrating the elimination of negative resistance.

This article has been accepted for publication in IEEE Transactions on Power Delivery. This is the author's version which has not been fully edited and content may change prior to final publication. Citation information: DOI 10.1109/TPWRD.2024.3466314

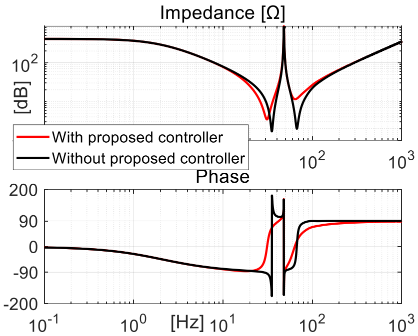

Fig. 23 Z_{MMC3} with and without proposed control.

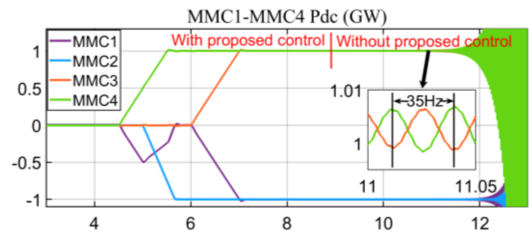

Fig. 24 Active power of MMC1-4 with and without proposed control.

Furthermore, Fig. 24 presents the active power of MMC1-4 with and without the proposed control in time domain simulation. Initially, with the proposed control, the performance of MMC3 is improved, leading to a stable system. However, after 9 s, MMC3 operates without the proposed controller and consequently, exhibits resonance with MMC4 at a frequency of 35 Hz, which further destabilizes the entire DC network. These simulation results confirm the effectiveness of the proposed controller and align with the analysis in Figs. 12 and 13.

C. Improving system stability with implementation of HTS cables

In Section IV C, the impedance model analysis reveals that the DC network becomes unstable when HTS cables are implemented. To mitigate this instability, the proposed zero-sequence controller is applied to both MMC3 and MMC4. The time domain simulation results are shown in Fig. 25. Before 9 s, the system with HTS cables operates stably under the proposed circulating current control. However, once the proposed circulating control is removed after 9 s, the system becomes unstable. This confirms the effectiveness of the proposed control strategy. Moreover, a closer examination of the zoomed-in portion of the waveforms reveals a resonant frequency of 33 Hz and the presence of ripple at 256 Hz, which align with the earlier analysis presented in Section IV C.

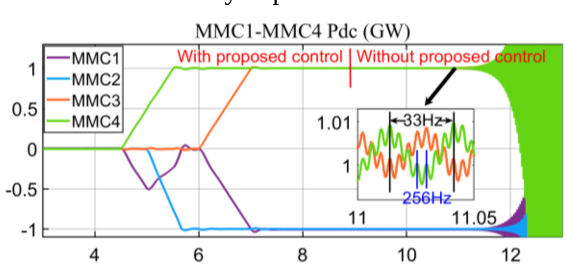

Fig. 25 Active power of MMC1-4 with HTS cables

D. Improving system stability under low transmitted power

To enhance system stability under conditions of low transmitted power, the proposed control is implemented for both MMC2 and MMC3 to reshape the DC impedances at the resonance frequency of 256 Hz, as shown in Figs. 18 and 19. The impedances Z_{MMC3} with different K values are shown in Fig. 26, where K = 0 represents the impedance without the proposed control. When K = 0, Z_{MMC3} is equal to $2(L_m+R_m)/3$, i.e., (0.05+j89.19) Ω. Thus, the magnitude of Z_{MMC3} is around 89, and the phase is around 90°. As K increases to 15, 30, and 45, the virtual resistance added to Z_{MMC3} increases accordingly to 10 Ω, 20 Ω, and 30 Ω, respectively, resulting in complex impedance values (10.05+j89.19) Ω, (20.05+j89.19) Ω, and (30.05+j89.19) Ω , with magnitudes around 90, 91, and 94, and phase angles of 84°, 77°, and 71°, respectively. These theoretical calculations align with the values observed in Fig. 26, confirming that the proposed control method effectively introduces virtual resistance in the high-frequency range, characterized by a value of 2K/3.

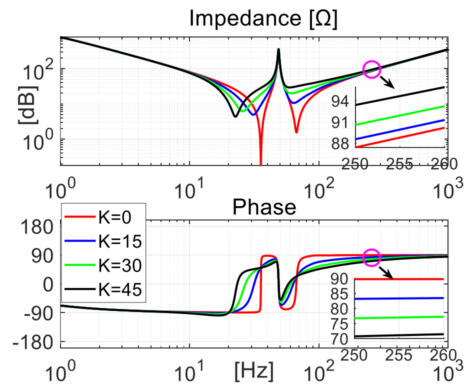

Fig. 26 Z_{MMC3} with proposed control using different K values.

Fig. 27 shows Z_{MMC3} and Z_{net3} with proposed control both using a gain K=30. Comparing these impedances to those shown in Fig. 18 reveals significant improvements: the phase of Z_{MMC3} is closer to 0° above 20 Hz, indicating increased damping. Additionally, with the proposed control applied to MMC2, the resonance magnitude of Z_{net3} decreases and the phase shift at the resonance frequency becomes smoother compared to Fig. 18, which results in Z_{net3} having a phase greater than -90° around 256 Hz. These enhancements in the phases of both Z_{MMC3} and Z_{net3} contribute to an overall improvement in system stability.

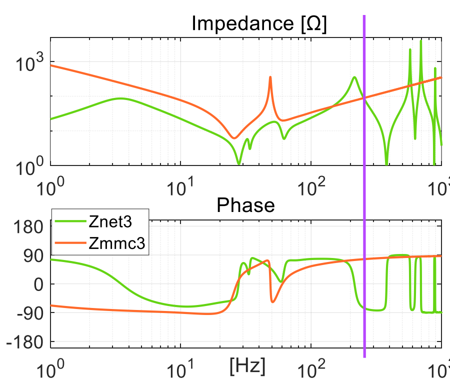

Fig. 27 Z_{MMC3} and Z_{net3} with proposed control.

This article has been accepted for publication in IEEE Transactions on Power Delivery. This is the author's version which has not been fully edited and content may change prior to final publication. Citation information: DOI 10.1109/TPWRD.2024.3466314

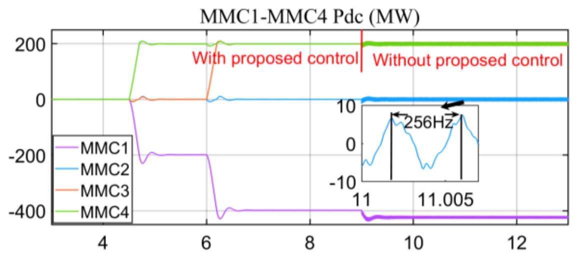

Fig. 28 Active power of MMC1-4 when MTDC transmits low power.

Fig. 28 depicts the results of the time-domain simulation. The system operates stably with the proposed control for MMC2 and MMC3 before 9 s. Subsequently, the proposed control is disabled, and a small disturbance is introduced. It is apparent that without the proposed control, the system resonates at 256 Hz. This reaffirms the effectiveness of the proposed control in improving the stability of the MTDC system under conditions of low transmitted power.

VI. Conclusion

This paper has developed a comprehensive DC impedance model for the MMC in the context of a four-terminal meshed DC network. Various types of controllers, including grid forming control for offshore stations connected to OWFs, DC and AC voltage control, PLL, inner current loop, and active power control, are considered and incorporated into the model. The DC impedance of the MMC is also derived for the different AC circuits for which the MMCs are connected with, such as AC grids and OWFs. Based on the impedance model, the stability of the four-terminal DC network is evaluated. The key findings of the study are as follows:

1. Comparing the three different types of active power controls, it is observed that P_{ac} with PI control has a similar control effect to feedforward control ($2P_{ref}/3v_d$) in terms of the DC active power response. P_{dc} with PI control exhibits a faster response even using lower PI parameters but can easily lead to stability issues.
2. The MMC controlling OWFs can introduce stability issues on the DC side within the MTDC system, particularly when they are in close proximity. The resistance of DC cables can help mitigating resonance and enhance system stability.
3. The implementation of HTS cables can exacerbate the stability issues in the DC network, unless mitigating control strategies are employed. HTS cables, characterized by their near-zero resistance, result in reduced damping for the DC system. In particular, at high frequencies (above 200 Hz), the resonance between the MMC and HTS cables exhibits minimal damping. This is attributed to the fact that the MMC impedance is approximately equal to $2(L_m+R_m)/3$, while HTS cables are unable to provide adequate damping effect. Mitigating control strategies have been demonstrated as relatively easy to implement for these effects.
4. The zero-sequence control of the circulating current plays a crucial role in shaping the DC impedance of the MMC. Accordingly, the MMC's DC impedance can be reshaped by introducing additional damping at specified frequency ranges to improve the overall system stability.

References

[1] S. Dehnath, J. Qin, B. Bahrani, M. Saeedifard, and P. Barbosa, “Operation, control, and applications of the modular multilevel converter: A review,” *IEEE Trans. Power Electron.*, vol. 30, no. 1, pp. 37–53, Jan. 2015.

[2] M. A. Perez, S. Bernet, J. Rodriguez, S. Kouro, and R. Lizana, “Circuit topologies, modeling, control schemes, and applications of modular multilevel converter,” *IEEE Trans. Power Electron.*, vol. 30, no. 1, pp. 4–17, Jan. 2015.

[3] C. Oates, “Modular multilevel converter design for VSC HVDC applications,” *IEEE J. Emerg. Sel. Topics Power Electron*., vol. 3, no. 2, pp. 505–515, Jun. 2015.

[4] X. Li, Q. Song, W. Liu, S. Xu, Z. Zhu, and X. Li, “Performance analysis and optimization of circulating current control for modular multilevel converter,” *IEEE Trans. Ind. Electron.*, vol. 63, no. 2, pp. 716–727, Feb.2016.

[5] H. Saad, Y. Fillion, S. Deschanvres, Y. Vernay, and S. Dennetière, “On resonances and harmonics in HVDC-MMC station connected to AC grid,” *IEEE Trans. Power Del.*, vol. 32, no. 3, pp. 1565–1573, Jun. 2017.

[6] S. Zhu, K. Liu, L Qin, X. Ran, Y. Li; Q. Huai, X. Liao, and J. Zhang, “Reduced-order dynamic model of modular multilevel converter in long time scale and its application in power system low frequency oscillation analysis,” *IEEE Trans. Power Del.*, vol. 34, no. 6, pp.2110–2122, Dec. 2019.

[7] A. M. C. Buchhagen, M. Greve, and J. Jung, “Harmonic stability practical experience of a TSO,” in Proc. Wind Integration Workshop, Nov. 2016, pp. 1–6.

[8] C. Zou et al., “Analysis of resonance between a VSC-HVDC converter and the AC grid,” *IEEE Trans. Power Electron.*, vol. 33, no. 12, pp. 10157–10168, Dec. 2018.

[9] J. Sun, “Small-Signal Methods for AC Distributed Power Systems–A Review,” *IEEE Transactions on Power Electron.*, vol. 24, no. 11, pp. 2545-2554, Nov. 2009.

[10] J. Lyu, X. Zhang, X. Cai, and M. Molinas, “Harmonic state-space based small-signal impedance modeling of modular multilevel converter with consideration of internal harmonic dynamics,” *IEEE Trans. Power Electron.*, vol. 34, no. 3, pp. 2134–2148, Mar. 2019.

[11] Y. Chen, L. Xu, A. Egea-Alvarez, B. Marshall, M. H. Rahman and A. D. Oluwole, “MMC impedance modelling and interaction of converters in close proximity,” *IEEE J. Emerging Sel. Top. Power Electron.*, vol. 9, no. 6, pp. 7223-7236, Dec. 2021.

[12] H. Wu and X. Wang, “Dynamic Impact of Zero-Sequence Circulating Current on Modular Multilevel Converters: Complex-Valued AC Impedance Modelling and Analysis,” *IEEE J. Emerg. Sel. Topics Power Electron.*, vol. 8, no. 2, pp. 1947-1963, June 2020.

[13] K. Ji, G. Tang, J. Yang, Y. Li, and D. Liu. “Harmonic stability analysis of MMC-based DC system using dc impedance model,” *IEEE J. Emerg. Sel. Topics Power Electron.*, vol. 8, no. 2, pp. 1152–1163, Jun. 2020.

[14] K. Ji, G. Tang, H. Pang and J. Yang, “Impedance Modeling and Analysis of MMC-HVDC for Offshore Wind Farm Integration,” *IEEE Trans. Power Del.*, vol. 35, no. 3, pp. 1488-1501, June 2020.

[15] Wu. Du, Q. Fu, and H. Wang, “Small-Signal stability of an AC/MTDC power system as affected by open-loop modal coupling between the VSCs,” *IEEE Trans. Power Syst.*, vol. 33, no. 3, pp. 3143–3152, May 2018.

[16] Q. Fu, W. Du, H. Wang, Z. Zheng and X. Xiao, “Impact of the Differences in VSC Average Model Parameters on the DC Voltage Critical Stability of an MTDC Power System,” *IEEE Trans. Power Syst.*, vol. 38, no. 3, pp. 2805-2819, May 2023.

[17] H. Zhang, X. Wang, M. Mehrabankhomartash, M. G. Saeedifard, Y. Meng, and X. Wang, “Harmonic stability assessment of multi-terminal DC (MTDC) systems based on the hybrid AC/DC admittance model and determinant-based GNC,” *IEEE Trans. Power Electron.*, vol. 37, no. 2, pp. 1653–1665, Feb. 2022.

[18] B. Zhang, X. Du, C. Du, J. Zhao, and F. Li, “Stability modeling of a three-terminal MMC-HVDC transmission system,” *IEEE Trans. Power Del.*, vol. 37, no. 3, pp. 1754–1763, Jun. 2022.

[19] Z. Li, Z. Wang, Y. Wang, T. Yin, N. Mei, B. Yue, and W. Lei, “Accurate impedance modeling and control strategy for improving the stability of dc system in Multiterminal MMC-Based DC grid,” *IEEE Trans. Power Electron.*, vol. 35, no. 10, pp. 10026–10047, Oct. 2020.

[20] K. Ji, G. Tang, J. Yang, Y. Li and D. Liu, “Harmonic Stability Analysis of MMC-Based DC System Using DC Impedance Model,” *IEEE J. Emerg. Sel. Topics Power Electron.*, vol. 8, no. 2, pp. 1152-1163, Jun. 2020.

[21] Charalambous, "Interference activity on pipeline systems from VSC-Based HVDC cable networks with earth/sea return: An insightful review," *IEEE Trans. Power Del.*, vol. 36, no. 3, pp. 1531–1541, Jun. 2021.
[22] B. Yang, J. Kang, S. Lee, C. Choi, and Y. Moon, "Qualification test of a 80 kV 500 MW HTS DC cable for applying into real grid," *IEEE Trans. Appl. Supercond.*, vol. 25, no. 3, pp. 1–5, Jun. 2015.
[23] A. Morandi, B. Gholizad, M. Stieneker, H. Stagge and R. W. De Doncker, "Technical and economical evaluation of DC high-temperature superconductor solutions for the grid connection of offshore wind parks," *IEEE Trans. Appl. Supercond.*, vol. 26, no. 6, pp. 1–10, Sept. 2016.
[24] M. C. Dinh et al., "Performance analysis of a model-sized superconducting DC transmission system based VSC-HVDC transmission technologies using RTDS," Physica C: Supercond. Appl., vol. 478, pp. 10–14, 2012
[25] K. Sharifabadi, L. Harnefors, H. Nee, S. Norrga, and R. Teodorescu, Design, control, and application of modular multilevel converters for HVDC transmission systems. Chichester, WS, UK: Wiley, 2016.
[26] W. Wang, A. Beddard, M. Barnes, and O. Marjanovic, "Analysis of active power control for VSC–HVDC," *IEEE Trans. Power Del.*, vol. 29, no. 4, pp. 1978–1988, Aug. 2014.
[27] T. M. Haileselassie and K. Uhlen, "Impact of DC line voltage drops on power flow of MTDC using droop control," *IEEE Trans. Power Syst.*, vol. 27, no. 3, pp. 1441–1449, Aug. 2012.
[28] G. Amico, A. Egea-Àlvarez, P. Brogan and S. Zhang, "Small-signal converter admittance in the pn-frame: systematic derivation and analysis of the cross-coupling terms," *IEEE Trans. Energy Conver.*, vol. 34, no. 4, pp. 1829-1838, Dec. 2019.
[29] J. Beerten, S. D'Arco, and J. A. Suul, "Frequency-dependent cable modelling for small-signal stability analysis of VSC-HVDC systems," *IET Generat., Transmiss. Distrib*., vol. 10, no. 6, pp. 1370–1381, 2016.
[30] B. Wen, D. Boroyevich, R. Burgos, P. Mattavelli and Z. Shen, "Inverse Nyquist Stability Criterion for Grid-Tied Inverters," *IEEE Trans. Power Electron.*, vol. 32, no. 2, pp. 1548-1556, Feb. 2017.
[31] J. Freytes, "Small-signal stability analysis of modular multilevel converters and application to MMC-based multi-terminal DC grids," Ph.D. dissertation, École centrale de Lille, Villeneuve-d'Ascq, France, 2017.
[32] S. Li, X. Wang, Z. Yao, T. Li, and Z. Peng, "Circulating current suppressing strategy for MMC-HVDC based on nonideal proportional resonant con trollers under unbalanced grid conditions," *IEEE Trans. Power Electron*., vol. 30, no. 1, pp. 387–397, Jan. 2015.
[33] B. Wen, D. Dong, D. Boroyevich, R. Burgos, P. Mattavelli, and Z. Shen, "Impedance-based analysis of grid-synchronization stability for three-phase paralleled converters," *IEEE Trans. Power Electron*., vol. 31, no. 1, pp. 26–38, Jan. 2016.
[34] W. Xiang, W. Yuan, L. Xu, E. Hodge, J. Fitzgerald, P. McKeever, and K.Bell, "DC fault study of a point-to-point HVDC system integrating offshore wind farm using high-temperature superconductor dc cables," *IEEE Trans. Energy Convers.*, vol. 37, no. 1, pp. 377–388, Mar. 2022.

Yin Chen received the B.S. degree in electrical engineering from Huazhong University of Science and Technology, Wuhan, China, in 2009, and the M.S. degree in electrical engineering from Zhejiang University, Hangzhou, China, in 2014. He received the Ph.D. degree in Electrical Engineering from University of Strathclyde, Glasgow, U.K., in 2020.
He is currently an associate researcher with University of Strathclyde in Glasgow, UK. His research interests include the modeling of power electronic converters, the technology of grid integration of new energy sources, and stability analysis of HVDC transmission systems.

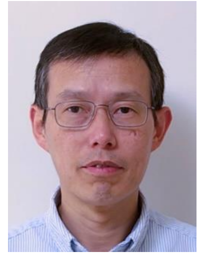

Lie Xu (Senior Member, IEEE) received the B.Sc. degree in mechatronics from Zhejiang University, Hangzhou, China, in 1993, and the Ph.D. degree in electrical engineering from the University of Sheffield, Sheffield, U.K., in 2000. He was with ALSTOM T&D Stafford and Queen's University of Belfast, U.K. In 2013, he joined the Department of Electronic & Electrical Engineering, University of Strathclyde, Glasgow, U.K. where he is currently a Professor. Since September 2024, he has also been with Mitsubishi Electric UK. His research interests include power electronics, wind energy generation and grid integration, HVDC and DC grid systems.

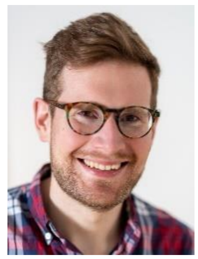

Agustí Egea-Àlvarez (S'12–M'14) obtained his B.Sc, MSc and Ph.D. from the Technical University of Catalonia in Barcelona in 2008, 2010 and 2014 respectively. In 2015 he was a Marie Curie fellow in the China Electric Power Research Institute (CEPRI). In 2016 he joined Siemens Gamesa as converter control engineer working on grid forming controllers and alternative HVDC schemes for offshore wind farms. Currently, he is a Professor at the Department of Electronic and Electrical Engineering and a member of the PEDEC (Power Electronics, Drives, and Energy Conversion) group at the University of Strathclyde, where he has been since 2018. He is a member of IEEE, IET and has been involved in several CIGRE and ENTSO-E working groups.
His current research interests include control and operation of high-voltage direct current systems, renewable generation systems, electrical machines and power converter control.

Eoin Hodge is the Chief Engineer at SuperNode, which is developing superconductor-based grid technologies. Previously, he has worked in technology leadership positions in offshore renewables technology and applied superconductivity R&D, developing power generation equipment and advanced grid protection systems for transmission networks. He holds an Engineering Master's degree from MTU in Ireland and PhD in Electrical Engineering from the University of Wollongong in Australia.

Shahab Sajedi is a PhD researcher at Technological University Dublin since 2016 and defended his thesis successfully in 2021. His research interests include FACTS, Active Power Filters, Dynamic Voltage Restorers, Unified Power Quality Conditioners, Inverters and Converters Topology and Control for various Power Electronics applications. His PhD research is in modelling and simulation of various Multi-Level Inverter topologies in the HVDC systems relating to their fault ride through capability. Currently he is working as a power system engineer in SuperNode.

Keith McCullough received his BEng in Electrical Power System Engineering from the Munster Technical University, Ireland, in 2012. He has worked internationally as a Senior Electrical Project Engineer in the Oil & Gas Industry leading the electrical design, development, manufacture, and testing of topside and subsea control systems. He has extensive experience in offshore engineering, LV distribution systems and PLC control systems.

His research interests include power systems engineering, generation and transmission product development.

Paul McKeever received the B.Eng. and M.Eng. degrees (Hons.) in electrical and electronic engineering from the University of Bradford, Bradford, U.K. In August 2006, he joined ORE Catapult (formerly Narec) and is currently the Head of Electrical Research. Prior to ORE Catapult, he spent 16 years with the automotive and railway industries as a Project Engineer, Lead Engineer and Technical Team Leader roles. His research team is responsible for the delivery of an electrical research programme ranging from wind turbine components to energy system/electrical infrastructure solutions. He is a Member of the Institution of Engineering and Technology and a Chartered Engineer (C.Eng). He currently holds the Board and ExCo positions with the European Association of Renewable Energy Research Centres, European Energy Research Alliance Joint Programme for Wind, and European Technology and Innovation Platform for Wind. He is also the Chair of the Industrial Advisory Board for the SuperGen ORE Hub research programme.

Michael Smailes received an M.Eng. (hons) in Electrical and Mechanical Engineering from The University of Edinburgh in 2011. He then received his D.Eng from The Universities of Edinburgh, Stathclyde and Exeter through the IDCORE programme in 2018 on Hybrid HVDC Transformers in multiterminal HVDC networks. Since 2016 Michael Smailes has worked in the Applied Research Team at ORE Catapult and became a Senior Research Engineer in grid integration in 2020. His research interests include new ancillary services for offshore renewables including, inertial, frequency and blackstart as well as novel grid compliance testing strategies. Michael has published numerous conference and journal articles and has an international patent on MMC converter control.